

The Influence of Phase Formation on Irradiation Tolerance in a Nanocrystalline TiZrNbHfTa Refractory High-Entropy Alloy

Michael Moschetti, Alan Xu, Anton Hohenwarter, Tao Wei, Joel Davis, Ken Short, Gordon J. Thorogood, Charlie Kong, Jean-Philippe Couzinié, Dhriti Bhattacharyya, Jamie J. Kruzic,* and Bernd Gludovatz*

Refractory high-entropy alloys (RHEAs) are candidate structural materials for nuclear applications due to their promising high-temperature mechanical performance and irradiation tolerance. However, most body-centered cubic (BCC) RHEAs form additional phases depending on their thermal history, with few studies assessing their effect on irradiation tolerance. This study characterizes the impact of phase transformations on the room-temperature irradiation tolerance of a nanocrystalline TiZrNbHfTa RHEA by assessing its microstructure and micromechanical properties before and after thermal treatments between 500 and 800 °C. The alloy demonstrates exceptional irradiation tolerance before and after 500 °C treatments for 1–100 h, which induce BCC to hexagonal close-packed (HCP) phase transformation, with excellent microstructural stability and minimal irradiation-induced hardening. Conversely, 800 °C treatment for 1 h forms two major BCC phases and a minor HCP phase, negatively impacting both pre- and post-irradiation mechanical performance and causing significant irradiation-induced hardening and embrittlement. Additionally, this research identifies a second HCP phase in the 500 °C, 100 h-treated condition, marking its first mention in the literature. This study emphasizes the importance of assessing temperature and phase formation effects on the irradiation tolerance of RHEAs for future nuclear reactors.


1. Introduction

Structural materials in current and future nuclear reactor designs must withstand extreme thermal, physical, chemical, and radiation-related challenges. While existing light water reactors typically operate at temperatures of ≈ 300 °C with water as the coolant,^[1] prospective future reactors may operate at temperatures of up to 1,000 °C, using a range of coolants such as supercritical water, liquid metals, molten salts, and gas.^[2] Additionally, components in nuclear reactors must withstand irradiation damage, with some components expected to reach up to 200 lifetime displacements per atom (dpa) promoting potential phase transformations, irradiation-induced hardening and swelling, irradiation-assisted creep, and stress-corrosion cracking.^[3]

High-entropy alloys (HEAs), which are commonly defined as alloys consisting of five or more elements mixed in equiatomic or near-equiatomic ratio,^[4] are a promising class of materials for nuclear applications as some alloys have been reported to exhibit exceptional combinations of mechanical, thermomechanical, and corrosion-tolerant properties.^[5–7] HEAs can additionally

M. Moschetti, J. J. Kruzic, B. Gludovatz
School of Mechanical and Manufacturing Engineering
University of New South Wales (UNSW Sydney)
Sydney, NSW 2052, Australia
E-mail: j.kruzic@unsw.edu.au; b.gludovatz@unsw.edu.au

A. Xu, D. Bhattacharyya
School of Materials Science and Engineering
University of New South Wales (UNSW Sydney)
Sydney, NSW 2052, Australia

 The ORCID identification number(s) for the author(s) of this article can be found under <https://doi.org/10.1002/adem.202300863>.

© 2023 The Authors. Advanced Engineering Materials published by Wiley-VCH GmbH. This is an open access article under the terms of the Creative Commons Attribution License, which permits use, distribution and reproduction in any medium, provided the original work is properly cited.

DOI: 10.1002/adem.202300863

A. Xu, T. Wei, J. Davis, K. Short, G. J. Thorogood, D. Bhattacharyya
Australian Nuclear Science and Technology Organisation (ANSTO)
New Illawarra Road, Lucas Heights, NSW 2234, Australia

A. Hohenwarter
Department of Materials Science
Montanuniversität Leoben
Jahnstrasse 12, Leoben 8700, Austria

C. Kong
Electron Microscope Unit
Mark Wainwright Analytical Centre
The University of New South Wales (UNSW Sydney)
Sydney, NSW 2052, Australia

J.-P. Couzinié
Université Paris Est Creteil, CNRS, ICMPE
UMR 7182 – 2 rue Henri Dunant, Thiais 94320, France

exhibit improved irradiation tolerance,^[8–15] with their high configurational entropy considered a key factor for such behavior, although its importance remains controversial.^[16] Nevertheless, the atomistic structures of HEAs can affect thermal conductivity,^[17,18] defect production, and defect migration,^[11] improving the irradiation-damage tolerance of these materials. One promising alloy for nuclear applications is the refractory HEA (RHEA) TiZrNbHfTa, which exhibits excellent strength and sufficient ductility for use as a structural material.^[8,19–21] Furthermore, this alloy comprises a body-centered cubic (BCC) structure, which typically provides improved irradiation-induced swelling resistance,^[22] and a refractory element constitution, which typically results in improved high-temperature mechanical performance.

In our prior work,^[8] a nanocrystalline (NC) TiZrNbHfTa RHEA, irradiated with He²⁺ ions to ≈ 0.8 dpa, demonstrated high microstructural stability and significantly reduced irradiation-induced hardening compared to conventional structural materials (e.g., 316 stainless steel, 45XD TiAl, and Zircaloy-4). However, Schuh et al.^[21] reported phase decomposition of the NC alloy at temperatures ranging from 500 to 900 °C, which are relevant to various next-generation nuclear applications. They observed the formation of additional hexagonal close-packed (HCP) and BCC phases upon thermal treatment at 500 and 800 °C for 1 h, respectively. Furthermore, during isothermal heat treatment at 500 °C for durations from 0.1 to 100 h, the material had a peak hardness after 1 h and a minimum hardness after 100 h. Both Stepanov et al.^[23] and Chen et al.^[24] made similar observations for coarse-grained (CG) TiZrNbHfTa. Combined, the two research groups studied a range of annealing treatments between 550 and 1000 °C for 1–192 h and reported the formation of additional HCP and BCC phases. Chen et al. noted that the intermediate-temperature (500–900 °C) phase stability of the RHEA needs to be better understood to make the alloy suitable for use in industry.

This study investigates the effects of the various phases that can form during thermal treatment of the TiZrNbHfTa RHEA on its room-temperature irradiation tolerance. The alloy is subjected to high-pressure torsion (HPT) processing to induce a NC structure, thermally treated between 500 and 800 °C for 1–100 h to induce the formation of additional phases with varying crystal structures, and irradiated with He²⁺ ions to ≈ 0.8 dpa. The alloy's microstructure and mechanical properties are then evaluated to further establish the alloy's potential as an irradiation damage-tolerant structural material for use in nuclear applications.

2. Experimental Section

The equiatomic TiZrNbHfTa HEA was synthesized by arc-melting raw materials with a purity of at least 99.9 wt% under an Ar atmosphere on a water-cooled Cu plate. The arc-melted material was homogenized by induction heating with electromagnetic stirring, then arc-melted once more before casting into a slug of ≈ 60 mm length and 8 mm diameter. Subsequently, the material was cold rolled to ≈ 1.3 mm thickness ($\approx 84\%$ reduction) and recrystallized at 1,100 °C for 5 h in a He atmosphere followed by fast cooling in the same environment. The HEA in the recrystallized state is hereafter referred to as the reX condition. The composition of the reX material was determined by

inductively coupled plasma atomic emission spectroscopy (ICP-AES) and LECO combustion.

Disks of 8 mm diameter were cut from the reX material using electrical discharge machining and processed by high-pressure torsion (HPT) under 7.8 GPa of pressure for 5 rotations at 0.2 rotations per minute, resulting in grain refinement to a NC size.^[21] As the mechanical test specimen dimensions are constrained by the shallow penetration depth of ion-irradiation (discussed later), such processing ensures a substantial number of grains across the specimens' critical dimensions, thereby more closely approximating the behavior of bulk polycrystalline material. The HEA in this state is referred to as the HPT condition. Segments of the HPT disks were placed into stainless steel foil "envelopes" with the edges twice-folded and peened, and heat-treated in an air furnace at either 500 or 800 °C for 1 h, or 500 °C for 100 h, before being water-quenched. These states are referred to as the 500°C|1h, 800°C|1h, and 500°C|100h conditions, respectively. The heat-treated samples were ground to remove at least 100 μ m from each face and polished with successively finer SiC sandpaper up to 4,000-grit followed by a final polishing step using a 0.04 μ m colloidal silica suspension. LECO combustion was performed on the HPT and 800°C|1h material to determine their oxygen content.

Specimens of each condition were irradiated with 5 MeV He²⁺ ions at a flux of 1.6×10^{12} ions cm⁻²s⁻¹ using the STAR Tandem Accelerator (CAS, ANSTO, Australia) until a fluence of 4.4×10^{17} ions cm⁻² was reached. A radially segmented degrader wheel consisting of 20 different thicknesses of Al ranging from 0.8 to 20 μ m was used to attenuate the incident ion energy, distributing dpa and implanted He across the depth of irradiation. While the temperature of the sample was not directly monitored during irradiation, prior experiments have shown that sample temperatures do not exceed ≈ 50 °C during irradiation.

Transmission electron microscopy (TEM) foils were extracted from specimens and thinned by focused ion beam (FIB)-milling in an Auriga 60 CrossBeam (Zeiss, Germany) instrument using Ga⁺-ions which was followed by final polishing in a NanoMill 1040 (Fischione Instruments, US) at successively lower voltages and currents until 450 eV and 200 μ A. Foils were extracted from midway between the disc centers and outer edges, where HPT-induced grain refinement has saturated.^[21] Specimen grain sizes and morphologies were characterized using a 2200FS (JEOL, Japan) TEM by bright- and dark-field imaging and selected-area diffraction (SAD) patterns. The distribution of irradiation-induced He-bubbles was determined by under- and over-focus imaging, with diameters determined by a linear regressive fit of off-focus measurements. Qualitative distributions and sizes of defects were obtained by placing specimens in a two-beam condition.

The crystal structures and lattice parameters of the HPT, 500°C|1h, and 800°C|1h conditions were characterized by X-ray diffraction (XRD) using an Empyrean diffractometer (Malvern Panalytical, UK) with Cu-K α radiation ($\lambda = 1.54056$ Å), a step size of 0.0130° 2 θ , and a 10 s acquisition time per step. The 500°C|100h condition was characterized by synchrotron XRD on the powder diffraction beamline of the Australian Synchrotron (ANSTO, Australia). The specimens were ground to ≈ 30 μ m thickness, removing unirradiated material, then wire-cut to < 300 μ m width and placed in a 0.3 mm

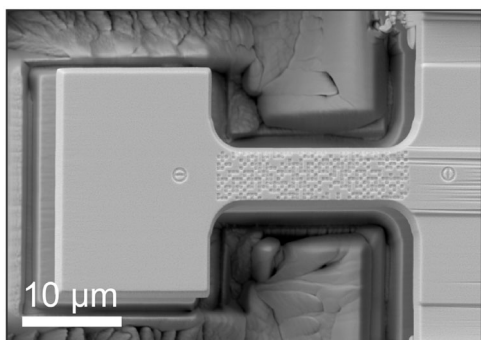


Figure 1. A dog bone microtensile test specimen with gauge dimensions of $\approx 5 \times 5 \times 16 \mu\text{m}^3$ and a checkered fiducial pattern on its surface.

capillary. Measurements were conducted at an energy of 21.004 keV ($\lambda = 0.590288 \text{ \AA}$), with a step size of $0.00376^\circ 2\theta$, and a total scan duration of 180 s. Phase fractions and lattice parameters were determined by applying Rietveld analysis using the HighScore Plus 5.1b (Panalytical, UK) and Topas (Bruker, MA, US) software packages, using LaB_6 as a standard for calibration.

Hardness was measured using a diamond Vickers tip on a Durascan-80 (Struers, Denmark) with a minimum of 14 indents for each material condition. Indents were carried out to a peak load of 100 mN, translating to a penetration depth ranging between 2.4 and $3.2 \mu\text{m}$. The dwell time for each indentation was 10 s. Dog bone-shaped microtensile specimens with gauge dimensions of $\approx 5 \times 5 \times 16 \mu\text{m}^3$ were prepared by FIB-milling with a checkered fiducial pattern on the surface (Figure 1). At least three specimens of each condition were tested in situ using an MTR-3 (MicroTesting Solutions, USA) microtensile testing rig inside an UltraPlus (Zeiss, Germany) scanning electron microscope (SEM). Tensile tests were conducted under displacement control at a displacement rate of $\approx 10 \text{ nm s}^{-1}$ while

incorporating regular 23 s pauses every 14 s to capture images. Strain was determined by digital image correlation (DIC) of the fiducial pattern using the GOM correlate software package (GOM Metrology, Germany), and load was recorded with a calibrated load cell. Specimens that failed outside of the gauge length were excluded from the results. Engineering stress–strain ($\sigma - \epsilon$)_{Eng} curves were individually fit to the Ramberg–Osgood equation, $\epsilon = \sigma/E + (\sigma/A)^b$, where E is Young's modulus, and A and b are material-dependent constants. Strain hardening exponents, n , were determined by fitting each true stress–strain ($\sigma - \epsilon$)_{True} curve to the Hollomon equation, $\sigma = K\epsilon^n$, where K is the strength coefficient. After failure, specimen fractography and energy dispersive X-ray (EDX) spectroscopy were performed using the Zeiss UltraPlus SEM and a JSM-7001F SEM (JEOL, Japan), respectively.

3. Results

3.1. Microstructure

The final composition of the reX material was measured to be $\text{Ti}_{20.67}\text{Zr}_{19.51}\text{Nb}_{19.28}\text{Hf}_{19.67}\text{Ta}_{20.78}$ (at%) with a trace amount of carbon (0.1 at%). The oxygen content of the material remained stable during thermal treatment, with the $800^\circ\text{C}|1\text{h}$ condition exhibiting a similar content (0.33 at%) to the HPT condition (0.35 at%) after $\approx 100 \mu\text{m}$ of material was removed from each surface.

Figure 2a presents the irradiation-induced dpa and He concentration as a function of depth, revealing a radiation-affected thickness of $\approx 12 \mu\text{m}$. The figure is adapted from our prior study,^[8] where detailed methodology can be found. Within the 2–10 μm range, both dpa and He concentration remain approximately plateaued at ≈ 0.8 and $\approx 0.75 \text{ at\%}$, respectively, with dpa exhibiting a slight decrease with increasing depth. The peaks observed in the figure result from the discrete energy attenuation caused by the 20 Al foils that comprise the degrader wheel. The

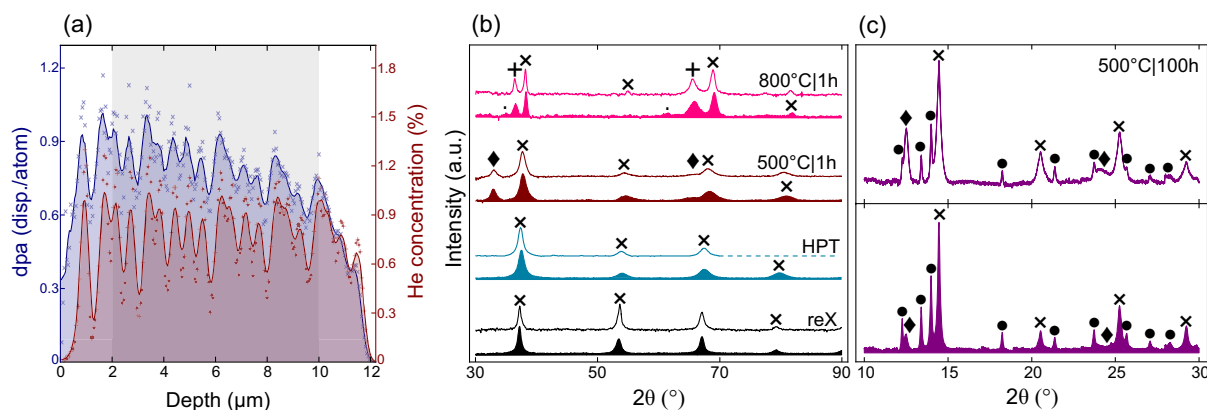


Figure 2. Phase evolution under various irradiation and thermal treatments. a) Displays the irradiation-induced damage profile, showing displacements per atom (dpa) and induced He concentration across the irradiated depth. The gray region indicates the approximately plateaued region from which micromechanical specimens were fabricated. Symbols and solid lines represent raw data and 5-point moving averages, respectively. b) Lab XRD results of the reX, HPT, $500^\circ\text{C}|1\text{h}$ and $800^\circ\text{C}|1\text{h}$ conditions, and c) synchrotron XRD results of the $500^\circ\text{C}|100\text{h}$ conditions. For both figures, unirradiated and irradiated states are represented by filled and unfilled spectra, respectively. Peaks identify BCC1/2 (x/+), and HCP1/2 (♦/●) phases. The dashed line for the irradiated HPT condition indicates a shorter scan, ending at $70^\circ 2\theta$. Minor peaks (.) in the unirradiated $800^\circ\text{C}|1\text{h}$ condition closely correspond to a Zr HCP phase; however, the absence of additional peaks leaves identification uncertain.

shallow penetration depth of He^{2+} -ion irradiation constrains the maximum size of micromechanical test specimens. In this study, the NC grain size of the HPT-processed material results in more grains across the critical dimensions of each test specimen, which better approximates the behavior of a bulk specimen. This is a distinct advantage of NC materials when conducting micromechanical tests.

Figure 2b,c and Table 1 display the phases present in each condition and irradiation state, along with their lattice parameters and phase weight fractions. A BCC phase is present in all conditions, accounting for 100% of the reX and HPT conditions, and $\approx 94\%$ of the $500^\circ\text{C}|1\text{h}$ condition. All heat-treated conditions possess an HCP phase, accounting for the remaining $\approx 6\%$ of the $500^\circ\text{C}|1\text{h}$ condition. These phases exhibit negligible irradiation-induced change. The $500^\circ\text{C}|100\text{h}$ condition was investigated by synchrotron XRD, which confirmed the presence of the previously reported BCC and HCP phases,^[21] with respective phase fractions of 87% and 11% in the unirradiated state and 92% and 5% in the irradiated state. Notably, a second HCP phase was identified in this condition, which, to the best of the authors' knowledge, has not previously been reported. In the unirradiated state, this new phase constitutes a minor phase fraction of 2.0%, a preferred orientation (expressed as multiples of a random distribution; MRD) in the radial direction of the HPT disks of $2.75 (\pm 0.06)$, and a lattice strain, ϵ_0 , of $0.48\% (\pm 0.06\%)$, while the irradiated state exhibits a greater phase fraction and preferred orientation of 3.4% and $6.90 (\pm 0.10)$, respectively, with a similar ϵ_0 , of $0.47\% (\pm 0.02\%)$. Supporting these findings, faint rings corresponding to the new HCP phase were observed in the associated SAD pattern; however, the phase was not identified during bright- and dark-field TEM imaging. Furthermore, it appears that XRD peaks corresponding to this phase are visible in the work of Stepanov et al.^[23] at $\approx 33^\circ$ and $66^\circ 2\theta$, although the latter peak is hard to distinguish as it is broad and partially overlaps with other peaks from the known HCP and BCC phases.

The $800^\circ\text{C}|1\text{h}$ condition comprises two distinct BCC phases with lattice parameters of ≈ 3.34 and 3.48 \AA and phase fractions of 60% and 40%, respectively, which remain approximately the same before and after irradiation. Schuh et al.^[21] identified these phases to be NbTa-rich and ZrHf-rich, respectively. Moreover, they predicted the existence of a ZrHf-rich HCP phase comprising 2% of the total microstructure using calculation of phase diagrams (CALPHAD) methodology; however, they were unable to observe this phase in TEM images due to its low volume fraction. This phase may be observed in minor peaks of the current study's *unirradiated* $800^\circ\text{C}|1\text{h}$ spectrum, although its presence is limited, leaving identification uncertain. No such peaks were observed in the $800^\circ\text{C}|1\text{h}$ *irradiated* counterpart.

As reported in our previous work,^[8] the reX condition has equiaxed grains of $\approx 80 \mu\text{m}$ size. Figure 3 shows the phase evolution and microstructures of the HPT, $500^\circ\text{C}|1\text{h}$, $500^\circ\text{C}|100\text{h}$, and $800^\circ\text{C}|1\text{h}$ conditions before and after irradiation. The unirradiated HPT condition exhibits a 2,000-fold grain refinement compared to the reX condition, with near-equiaxed grains of $\approx 40 \text{ nm}$. TEM analysis of the condition shows grains with uneven intragranular contrast and diffuse grain boundaries (GBs), suggesting a high dislocation density and significant dislocation-mediated lattice strain.^[25] The unirradiated $500^\circ\text{C}|1\text{h}$ condition shows no evident grain growth compared to its HPT counterpart and exhibits a reduced, but still significant, intragranular contrast variation with more clearly defined GBs, suggesting partial lattice relaxation and a reduced dislocation density. It should be noted that the diffuse GBs and uneven intragranular contrast result in uncertain grain statistics and, subsequently, a minor grain size increase of the $500^\circ\text{C}|1\text{h}$ condition may be unaccounted for. The unirradiated $500^\circ\text{C}|100\text{h}$ and $800^\circ\text{C}|1\text{h}$ conditions both exhibit grain growth, resulting in grain sizes of ≈ 100 and 200 nm , respectively, and further lattice relaxation identified by a greater contrast consistency within grains and across GBs. The irradiated states of all studied conditions are seen in Figure 3e–h, exhibiting no observed change of grain

Table 1. Microstructural and phase parameters, including average grain size, phases present, and their associated lattice parameters for each condition of both the unirradiated (U) and irradiated (I) states. Standard deviation is expressed in parentheses in terms of the least significant digit. Note: A standard deviation denoted as (0) does not imply the absence of uncertainty, but rather that such uncertainty falls below the decimal place of the reported significant figures.

	Grain size		BCC1		BCC2		HCP1			HCP2		
			<i>a</i> [Å]	[wt%]	<i>a</i> [Å]	[wt%]	<i>a</i> [Å]	<i>c</i> [Å]	[wt%]	<i>a</i> [Å]	<i>c</i> [Å]	[wt%]
ReX	80 μm	U	3.42 (0)	100	–	–	–	–	–	–	–	–
		I	3.42 (0)	100	–	–	–	–	–	–	–	–
HPT	40 nm	U	3.40 (0)	100	–	–	–	–	–	–	–	–
		I	3.40 (0)	100	–	–	–	–	–	–	–	–
$500^\circ\text{C} 1\text{h}$	40 nm	U	3.36 (2)	94 (1)	–	–	3.14 (2)	5.03 (2)	6 (1)	–	–	–
		I	3.37 (1)	93 (2)	–	–	3.14 (2)	4.95 (1)	7 (1)	–	–	–
$500^\circ\text{C} 100\text{h}^{\text{a})}$	100 nm	U	3.32 (0)	87 (8)	–	–	3.19 (0)	5.06 (0)	11 (7)	3.27 (0)	5.43 (0)	2.0 (14)
		I	3.32 (0)	92 (1)	–	–	3.19 (0)	5.07 (0)	5 (0)	3.32 (0)	5.42 (0)	3.4 (7)
$800^\circ\text{C} 1\text{h}$	200 nm	U	3.33 (0)	60 (2)	3.47 (0)	40 (3)	N/A ^{b)}			–	–	–
		I	3.34 (0)	60 (1)	3.49 (0)	40 (0)	N/A ^{b)}			–	–	–

^{a)}Determined by synchrotron XRD. Weighted profile R-values (RWP) and Goodness of Fit (GoF) are 4.6 and 2.8, 4.3 and 2.5 for the unirradiated and irradiated states, respectively. ^{b)}Due to uncertain identification of a potential HCP phase in the unirradiated $800^\circ\text{C}|100\text{h}$ specimen, its lattice parameters are labeled N/A.

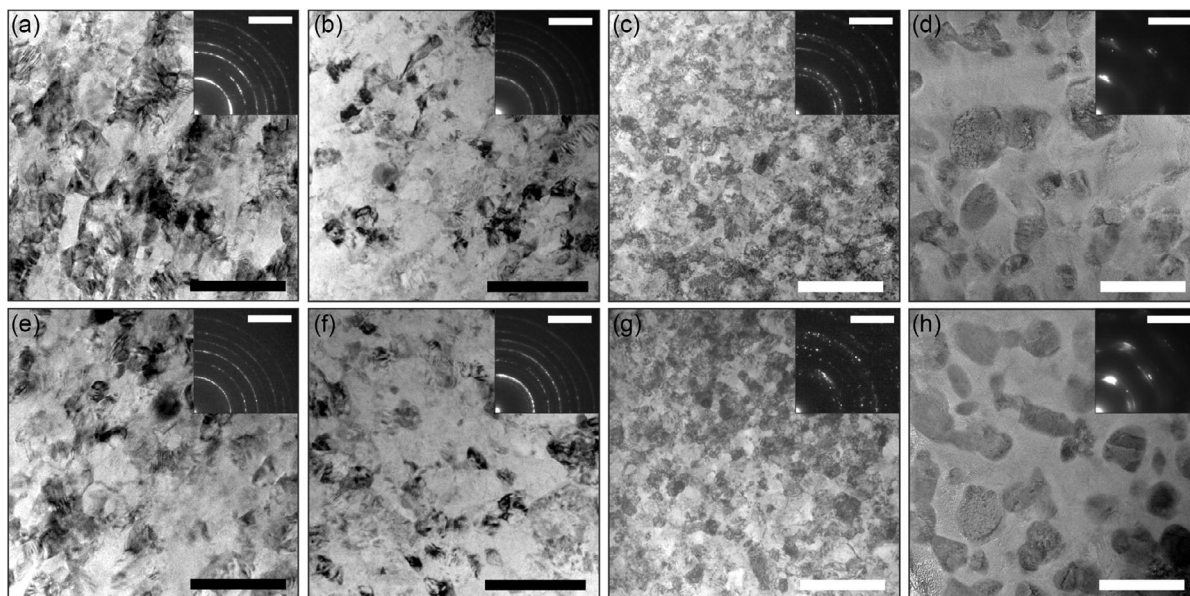


Figure 3. Microstructure of TiZrNbHfTa specimens by bright-field TEM imaging of a–d) unirradiated, and e–h) irradiated specimens, across various thermomechanical treatments, including the (a,e) HPT condition. Reproduced with permission.^[8] Copyright 2019, Springer Nature. (b,f) 500°C|1h condition, (c,g) 500°C|100h condition, and (d,h) 800°C|1h condition. Black scale bars = 100 nm. White scale bars = 500 nm. Insets show the respective selected-area diffraction (SAD) patterns with scale bars = 5 nm^{−1}.

size or grain texture compared to their unirradiated counterparts. In both irradiation states of the 800°C|1h condition (Figure 3d,h) lighter ZrHf-rich (BCC1) and darker NbTa-rich (BCC2) grains distinguish the two major phases. Note that in the 500 °C conditions, the contrast variation primarily highlights grain orientation rather than the differing phases, due to both the relatively minor HCP phase fraction and the reduced Z-contrast difference between the phases.

Figure 4a,b shows Fresnel fringes indicative of agglomerated helium in the form of bubbles in the irradiated HPT and 800°C|1h conditions, respectively. The He-bubbles in the HPT condition have diameters of ≈ 0.53 nm and are found preferentially located along GBs, whereas in the 800°C|1h condition, the bubbles have diameters of ≈ 0.71 nm and are distributed more uniformly throughout the grains. The distribution of He-bubbles in the 500°C|1h and 500°C|100h conditions, not shown here, exhibit a reduced preference for GBs with increasing grain size. The He-bubbles are homogeneously distributed across the entire ≈ 10 μ m depth of the TEM foils, suggesting uniform irradiation of the material. Figure 4c,d shows the reX condition before and after irradiation, respectively, using a two-beam imaging mode that highlights the crystallographic defects in black. In the unirradiated state, black dots of ≈ 1 –3 nm diameter are evenly distributed and distinct from each other. These black dots are likely to have been induced by FIB damage. Conversely, in the irradiated state, the black dots are larger, often exceeding 10 nm in diameter, and frequently intersect with each other. Notably, several ≈ 8 nm diameter dislocation loops are observed, as shown in Figure 4d. Due to limitations in the characterization methods employed and the complex microstructural features present in the material, especially in the conditions with the smallest grains,

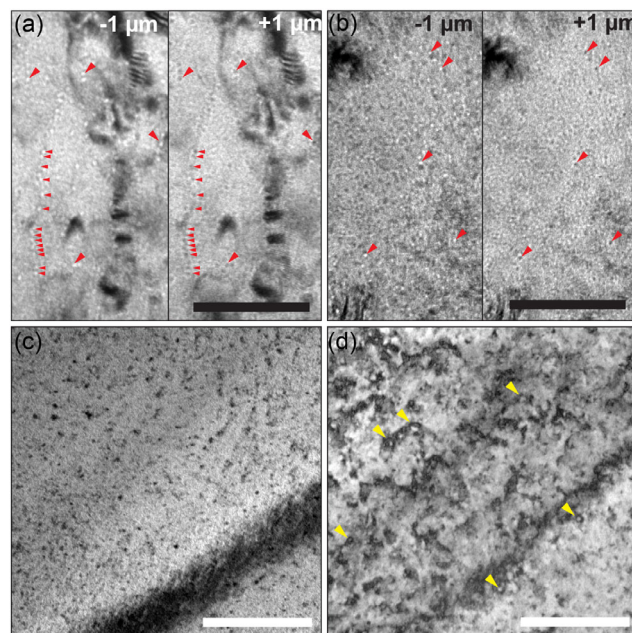


Figure 4. Irradiation-induced He-bubble and defect cluster formation. He-bubbles in the irradiated a) HPT, and b) 800°C|1h conditions are visible as white and black dots in under- and overfocus conditions ($-/+ 1$ μ m focus shift) as shown on the left and right sides of the split subfigure, respectively. The red arrows indicate several prominent bubbles. The growth of black dot damage is observed in the reX condition c) before, and d) after irradiation, using two-beam imaging to emphasize defects. Several dislocation loops are observed in the irradiated condition, indicated by yellow arrows. The dark bands crossing (c,d) are bend contours. Black scale bars = 50 nm. White scale bars = 100 nm.

the He-bubble and defect densities were not possible to determine quantitatively.

3.2. Micromechanical Properties

Figure 5 displays the tensile stress–strain curves of the investigated NC RHEA, while **Figure 6** and **Table 2** summarize its key mechanical properties and grain size.

No macromechanical tests were performed in the current study; however, Chen et al.^[26] studied a CG TiZrNbHfTa RHEA processed near-identically to that of the current study, reporting a tensile yield strength (YS) of 972 MPa, an ultimate tensile strength (UTS) of 1,000 MPa, and an elongation failure (EF) strain of 12.6%. Compared to this, the unirradiated HPT condition exhibits significant strengthening, with higher YS (1911 (± 92) MPa; +97%), UTS (2338 (± 97) MPa; +134%), and hardness (5.1 GPa; +42%). However, this improvement in strength comes with the typical Hall–Petch strengthening sacrifice of ductility, with a lower EF (4.3% ($\pm 0.6\%$); –66%). Compared to the unirradiated HPT condition, thermal treatment at 500°C|1h and 500°C|100h shows an increased EF (26% and 33%, respectively), with little change in tensile YS (+6% and –8%, respectively), and only the 500°C|1h condition

showing a higher hardness (12%). Conversely, comparing the unirradiated 800°C|1h condition to its HPT counterpart reveals a minor reduction in hardness (–3%), and larger reductions in tensile YS (–17%) and EF (–28%).

Irradiation of the reX, HPT, 500°C|1h, and 500°C|100h conditions results in moderate irradiation-induced hardness increases, ranging from 2% to 16%. In contrast, the 800°C|1h condition shows a much larger increase of 34%. The strain hardening exponents, n , of the unirradiated and irradiated states of the HPT condition are 0.089 ± 0.003 and 0.042 ± 0.006 , revealing an irradiation-induced reduction of 54%. Due to the premature failure of many of the thermally-treated samples, a reliable quantitative comparison of UTS, and hence strain hardening, between these conditions is not feasible.

The HPT, 500°C|1h, and 800°C|1h conditions show a similar irradiation-induced increase in YS of 15%, 15%, and 17%, respectively, while the 500°C|100h condition shows an increase of 5%. Irradiation also causes reductions in EF for all thermally treated conditions, with greater reductions seen in conditions treated for longer durations and at higher temperatures. The 500°C|100h and 800°C|1h conditions show 44% and 32% reductions in EF after irradiation, respectively. The HPT condition is an exception to this trend, showing a 16% increase in EF after irradiation.

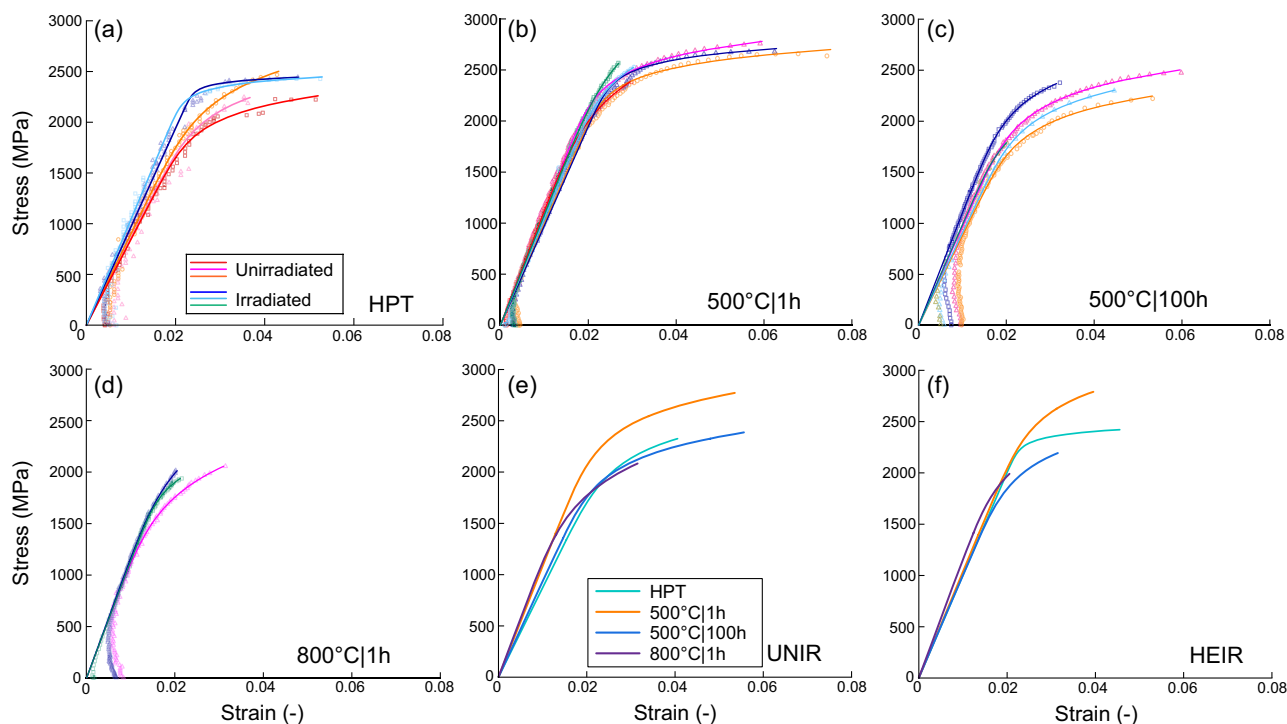


Figure 5. Tensile stress–strain characteristics of the NC TiZrNbHfTa RHEA. a–d) Show engineering tensile stress–strain curves for the HPT, 500°C|1h, 500°C|100h, and 800°C|1h conditions, respectively. The legend in (a) applies to all four conditions (a–d). Raw data are represented by symbols; solid lines indicate Ramberg–Osgood fits. e,f) Reorganization of the same data according to the unirradiated and irradiated states, respectively, where each curve corresponds the average of all tests for each unique combination of thermal treatment condition and irradiation state. The legend in (e) also applies to (f). HPT data reproduced with permission.^[8] Copyright 2019, Springer Nature. In a previous publication,^[8] the reported tensile data for the HPT condition showed slightly different values. These discrepancies, which account for less than a 10% difference in each of the key tensile properties listed in Table 2, resulted from measurements of cross-sections using SEMs with inconsistent calibrations. This issue has been addressed and corrected for in the current article.

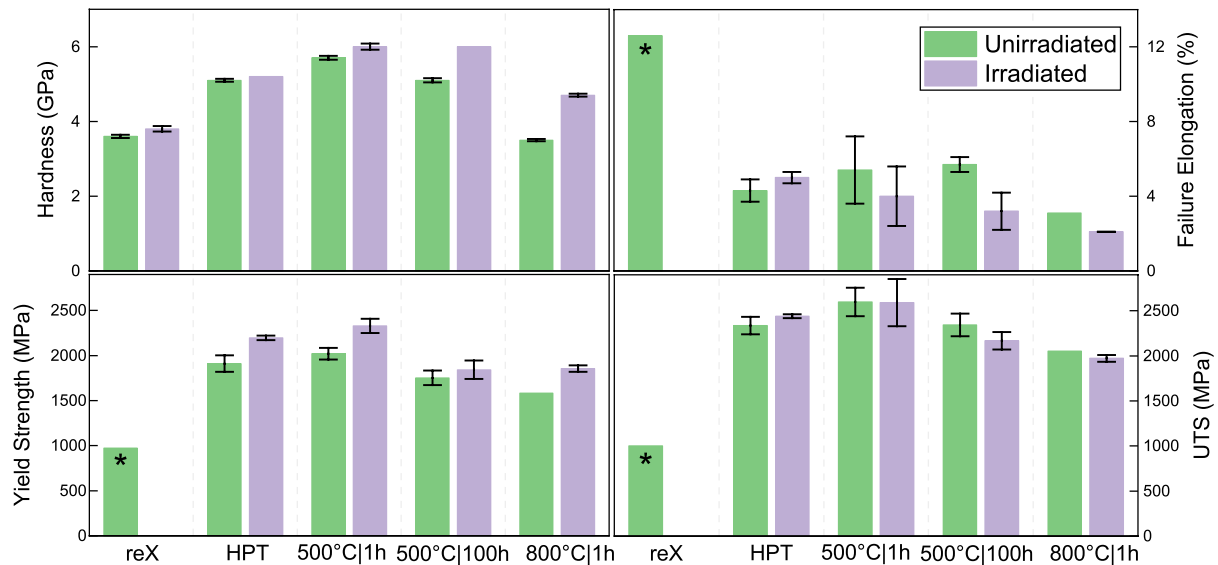


Figure 6. Mechanical properties in terms of hardness, failure elongation, yield strength, and ultimate tensile strength of the NC TiZrNbHfTa RHEA. Error bars denote standard deviation. * denotes values from Chen et al.^[26]

Table 2. Summary of key mechanical properties. GS represents grain size. Δ_i indicates the percent difference between irradiation states. # indicates the number of tests per result. Standard deviation is expressed in parentheses in terms of the least significant digit(s). Note: A standard deviation denoted as (0) does not imply the absence of uncertainty, but rather that such uncertainty falls below the decimal place of the reported significant figures.

		GS [μm]	Hardness [GPa]	Tensile properties				
				#	Yield strength $\sigma_{0.2\%}$ [MPa]	Ultimate strength [MPa]	Failure elongation [%]	Young's modulus [GPa]
ReX	Unirr.	80	3.6 (0)	–	972 ^{b)}	1000 ^{b)}	12.6 ^{b)}	–
	Irrad.		3.8 (1)	–	–	–	–	–
	Δ_i [%]		6.1	–	–	–	–	–
HPT	Unirr.	0.04	5.1 (0)	3	1911 (92)	2338 (97)	4.3 (0.6)	86.7 (1.6)
	Irrad.		5.2 ^{a)}	2	2196 (24)	2441 (21)	5.0 (0.3)	103.2 (3.2)
	Δ_i [%]		2.5	–	14.9	4.4	16.3	19.0
500°C 1h	Unirr.	0.04	5.7 (1)	3	2020 (65)	2600 (158)	5.4 (1.8)	110.8 (3.9)
	Irrad.		6.0 (1)	3	2330 (80)	2591 (262)	4.0 (1.6)	104.3 (2.6)
	Δ_i [%]		6.0	–	15.3	–0.3	–25.9	–5.9
500°C 100h	Unirr.	0.1	5.1 (1)	2	1753 (82)	2344 (126)	5.7 (0.4)	104.9 (3.9)
	Irrad.		6.0 ^{a)}	3	1843 (104)	2168 (96)	3.2 (1.0)	101.6 (7.3)
	Δ_i [%]		16.2	–	5.1	–7.5	–43.9	–3.1
800°C 1h	Unirr.	0.2	3.5 (0)	1	1582	2054	3.1	111.5
	Irrad.		4.7 (0)	2	1855 (35)	1973 (38)	2.1 (0)	114.9 (1.1)
	Δ_i [%]		33.6	–	17.3	–3.9	–32.3	3.0

^{a)}Values calculated by adjusting experimentally-determined continuous stiffness measurement (CSM)-method indentation results (not included) by –15.6%. This value represents the average difference between the hardness measurement methods for all other specimens. These differences align well with those reported by Jia et al.^[47]

^{b)}Values from Chen et al.^[26]

Post-test fracture surfaces of the tensile specimens are shown in **Figure 7**. The unirradiated HPT specimen exhibits a smooth surface with several pronounced ridges suggesting transgranular fracture. Failure in these specimens occurred $\approx 45^\circ$ from the loading direction. In contrast, the irradiated specimens display

a rough fracture surface characterized by grain pullout, dimple formation, and more sizeable pulled-out regions, indicating a transition toward intergranular fracture, as reported in our prior study.^[8] The heat-treated tensile specimens feature a granular structure with sizes corresponding to each condition's grain

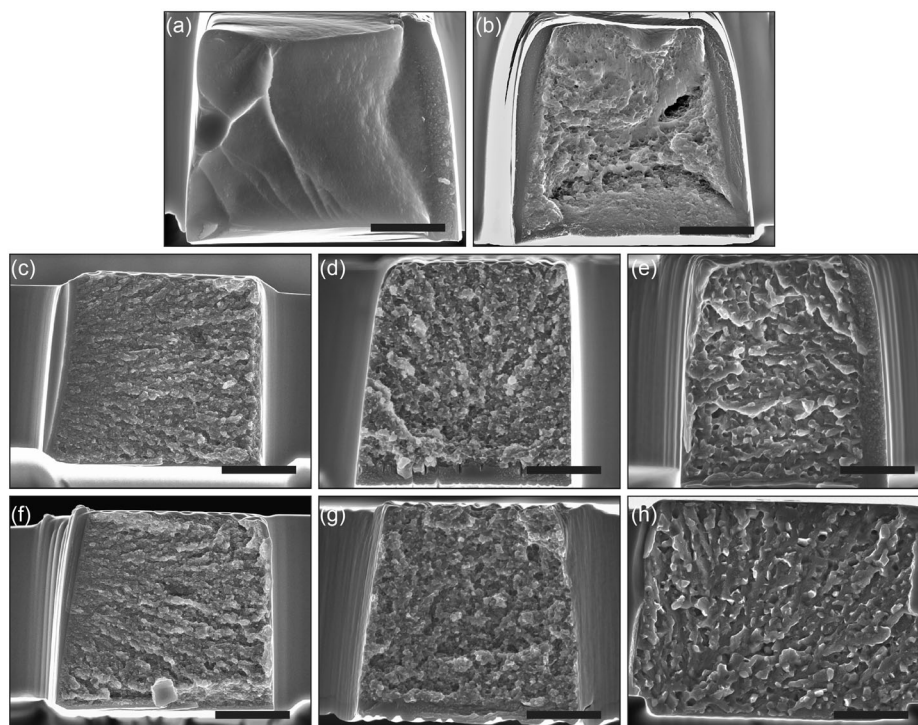


Figure 7. Microtensile fracture surfaces, showing the a,b) HPT condition. Reproduced with permission.^[8] Copyright 2019, Springer Nature. c–e) show the unirradiated states of the 500°C|1h, 500°C|100h, and 800°C|1h conditions, respectively, while f–h) show their irradiated counterparts. Scale bars = 2 μm.

size, and without signs of large-scale transcrystalline fracture (e.g., river patterns), indicating the occurrence of intergranular fracture. The fracture surfaces of the 500°C|1h specimens exhibit a directionality to their fracture, likely caused by a slight misalignment during testing. Enhanced magnification images of fracture surfaces for the 800°C|1h specimens are shown in **Figure 8**. Whole grains are visible in both irradiation states, with those of the unirradiated state displaying small-scale ridges both along their edges and on their surfaces. In contrast, the irradiated state exhibits a bimodal fracture surface, comprising both whole grains with smooth, faceted surfaces and sections of rough,

irregular surface. The elemental distribution—normalized per element such that the average values were set to 1—in **Figure 8c**, reveals the whole grains to be NbTa-rich, and the rough, irregular surfaces to be ZrHf-rich.

4. Discussion

4.1. Pre-irradiation

The hardness of the unirradiated reX condition (3.6 GPa) aligns closely with that reported by Senkov and Semiatin,^[27]

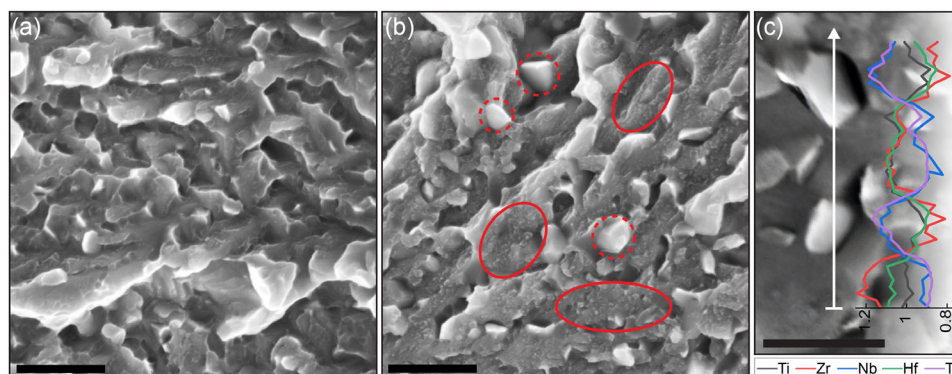


Figure 8. High-magnification microtensile fracture surfaces of the 800°C|1h condition for a) unirradiated, and b,c) irradiated states. Solid and dashed circles in (b) highlight sections of rough, irregular surface and whole grains, respectively. (c) The EDX-determined elemental distribution linescan taken along the white line, normalized per each element such that their average values were set to 1. Scale bars = 500 nm.

who determined a hardness of 3.4 GPa for a similarly processed TiZrNbHfTa RHEA. HPT-processing of the alloy leads to significant grain refinement (Table 1), increasing the GB density, while simultaneously increasing dislocation density and dislocation-mediated lattice strains, as shown by the complex intragranular contrast variations in Figure 3a. Consequently, YS, UTS, and hardness are substantially increased compared to the CG reX condition, albeit at the expense of reduced ductility (Table 2). Furthermore, the refinement of grains to NC dimensions ensures a sufficient number of grains over the cross-section of each specimen, better representing bulk polycrystalline material. Even with the largest grain size of 200 nm, as observed in the 800°C|1h condition, ≈ 25 grains span the 5 μm wide and thick tensile specimens, providing representative mechanical behavior.

Thermal treatment of the investigated RHEA typically results in grain growth and the formation of additional phases (Table 1). This process occurs more rapidly in NC alloys due to the numerous defects and GBs, which serve as fast diffusion pathways and preferred nucleation sites.^[28–30] Both the 500°C|100h and 800°C|1h conditions display grain growth and relaxation of the intragranular stresses, as shown by progressively reduced uneven intragranular contrast and sharper GB definition (Figure 3b). Despite no observable change to grain size in the 500°C|1h condition, the growth observed in its 500°C|100h counterpart likely indicates that grain growth is indeed occurring, albeit minimally, and thus not easily detected. Nevertheless, a slight decrease in uneven intragranular contrast and slightly more distinct GBs in the 500°C|1h condition, compared to the HPT condition, indicates stress-relaxation through a reduction of defect density within the individual grains and a decrease of grain boundary-free volume and dislocation pile-ups.^[31] Both phenomena are facilitated by the applied thermal treatment, which supplies sufficient energy for defect migration and recombination, as well as enabling GBs to achieve a more energetically favorable configuration.

The 500°C|1h condition also exhibits a partial transformation of the BCC phase into an HCP phase, as well as chemical segregation (Figure 2b and Table 1). The increased hardness and YS in this condition (Table 2) can likely be attributed to the formation of this HCP phase, as HCP structures are typically harder and more brittle than BCC structures due to their lower symmetry and fewer available slip systems.^[32,33] Conversely, the slight increase in ductility (Table 2) may be attributed to the thermally-induced reduction of defects and subsequent relaxation of the lattice, and a decrease of GB free volume and dislocation pile-ups which often serve as initiation points for failure. As there are no typical signs of phase precipitation, such as smaller crystals or the formation of the new phase along existing grain boundaries, the formation of the HCP phase likely occurs through phase transformation directly from the BCC phase, a phenomenon commonly observed in Group 4 metals such as Ti, Zr, and Hf.

The unirradiated 500°C|100h condition shows changes similar to its 500°C|1h counterpart, with an increased HCP phase fraction (Table 1), further reduction of lattice stresses and defect density, and enhanced chemical segregation resulting in reduced solid solution hardening, all of which can be attributed to the longer thermal treatment. Additionally, the 500°C|100h

condition shows grain growth, with grain size increasing from 40 to 100 nm. As per the Hall–Petch relationship, grain growth results in 10% and 13% reductions in hardness and YS, respectively, of the unirradiated 500°C|100h condition compared to its 500°C|1h counterpart (Table 2). In contrast to Schuh et al.'s^[21] near-equal BCC1:HCP1 weight ratio of 48:52, the ratio in our work is 87:11, with the remaining 2 wt% attributed to the new HCP2 phase. Given that Schuh et al.'s phase fractions were derived from CALPHAD, the difference could suggest that the 500°C|100h condition here, subjected to a relatively low homologous temperature, has not yet achieved the thermodynamic equilibrium that CALPHAD predicts. The phase weight fractions for the 800°C|1h condition align closely.

The unirradiated 800°C|1h condition displays the largest grain size and the least strain-related intragranular contrast, indicating that the elevated temperature of this annealing treatment results in pronounced defect migration leading to the most stress-relieved lattice among the HPT-processed conditions (Table 1). Consequently, this results in a further decrease in hardness and YS compared to the HPT and both 500°C-treated conditions (Table 2). Furthermore, the observed poor ductility of this condition implies embrittlement, which is attributed to the formation of an additional BCC phase. This may be due to weak GB cohesion or stress concentrations induced by elastic incompatibilities between phases. The reduced hardness of the condition, which is also lower than the CG reX condition, is attributed to the segregation of phases. As the Nb and Ta atoms exhibit similar atomic sizes of 198 and 200 pm, respectively, and so do the Zr and Hf atoms with sizes of 206 and 208 pm, their segregation into separate ZrHf-rich and NbTa-rich phases reduces the atomic misfit of the lattice and weakens solid-solution strengthening, leading to a softer material. Similar observations were made by Schuh et al.,^[21] who synthesized each of the ZrHf-rich and NbTa-rich phases separately, finding each to be softer than the original alloy (2.8 and 2.6 GPa, compared to 3.0 GPa, respectively).

4.2. Post-irradiation

The NC TiZrNbHfTa RHEA demonstrates excellent microstructural stability across all examined thermomechanical treatments when subjected to ≈ 0.8 dpa irradiation. Despite the numerous defects and GBs introduced by HPT processing, which can trigger grain growth and phase precipitation, no such changes were observed after irradiation and the lattice parameter remained approximately constant (Table 1). HPT-induced defects and the large fraction of GBs in NC materials can also act as sinks, assisting in the annihilation of irradiation-induced defects.^[34,35] This microstructural stability is a highly desirable characteristic that can help maintain mechanical performance during reactor operations, reducing the risk of significant irradiation-induced material degradation.

Despite the excellent overall microstructural stability, two irradiation-induced microstructural phenomena were observed in the studied RHEA: He-bubbles and black dot damage. He-bubbles form due to ion implantation during He²⁺-irradiation. The implanted He atoms, which have limited solubility in most metals,^[36] tend to diffuse and cluster within the material, leading

to the formation of He gas bubbles. These bubbles were observed in all irradiated conditions (Figure 4a,b), showing a preference for GBs, which act as sinks for He and facilitate the nucleation and growth of He-bubbles.^[37] Prior studies observed a bubble-denuded region extending 30–50 nm from GBs, attributed to preferential bubble migration.^[37,38] In the HPT condition, where most He-bubbles were observed at GBs, the small grain diameters of 40 nm may be considered entirely encompassed by such a bubble-denuded region, although a fraction of bubbles does appear to exist away from the GBs of the alloy. The preference of He-bubbles for GBs decreases with increasing grain size until a nearly even distribution of bubbles was observed in the 800°C|1h condition.

These bubbles act as obstacles to dislocation motion, causing hardening, embrittlement, and reducing ductility. Furthermore, these bubbles can act as stress concentrations, leading to microcracking and the development of voids and swelling,^[39] compromising the material's toughness and dimensional stability. He-bubbles occur due to the interaction of vacancies and implanted helium. The HEA-specific irradiation-tolerance phenomena (i.e., significant lattice distortion, complex energy landscape, and localized thermal spikes) may mitigate the formation of defects and promote their recombination, which would reduce their impact on mechanical properties, and reduce the number of vacancies available to accommodate He.^[40]

The high density of black dot damage in the irradiated TiZrNbHfTa RHEA (Figure 4d) is indicative of the introduction and growth of irradiation-induced defects, such as point defects and defect clusters. As these defects aggregate, they result in local lattice distortions, manifesting as characteristic dark spots in TEM images. The presence of dislocation loops, ≈ 8 nm in diameter, was also observed, similar in size to those found in a FeCrAl alloy exposed to 1 MeV Kr²⁺-ion irradiation up to 2.5 dpa at 320 °C.^[41] The accumulation and aggregation of irradiation-induced defects can impede dislocation mobility, leading to material hardening and embrittlement. The observed dislocation loops impede dislocation motion and contribute to the material's hardening and embrittlement. Interestingly, the unirradiated state also displayed smaller black dot damage (Figure 4c), which is atypical for unirradiated materials. This could suggest that some FIB damage occurred during specimen polishing, despite the use of the low voltage, low current polishing procedures.^[42]

The results of micromechanical testing (Figure 5, 6 and Table 2) show that irradiation of the TiZrNbHfTa RHEA generally leads to an increase in hardness and YS, but a decrease in ductility. This is due to the generation of lattice defects, such as point defects, dislocations, voids, and interstitial loops, as well as the introduction of He bubbles. These irradiation-induced defects, in combination with the additional defects and increased GB density induced by HPT processing, lead to a range of complex defect–defect and defect–GB interactions. Generally, these interactions obstruct atomic motion, causing the observed increase in strength and hardness, and a decrease in ductility (i.e., irradiation-induced hardening and embrittlement). The irradiation-induced hardness increases of 2.5%, 6.0%, and 16.2% in the HPT, 500°C|1h, and 500°C|100h conditions, are considerably lower than other commercial alloys, such as 316 stainless steel, 45XD TiAl, and Zircaloy-4, which exhibit hardness increases of 40–50%^[8] when irradiated under similar conditions.

The 800°C|1h condition has both the lowest pre-irradiation hardness and the highest irradiation-induced increase in hardness (Table 2). This significant difference is likely due to a combination of its annealing-induced reduction of defect density and the presence of a second BCC phase. Unlike the HPT condition, which exhibits a steady state of grain refinement that indicates defect saturation (i.e., further HPT-processing does not result in further grain refinement), the 800°C|1h condition exhibits a stress-relaxed microstructure which facilitates both its reduced pre-irradiation hardness and greater capacity to accommodate new defects. Consequently, this condition experiences a proportionally larger increase in hardness due to irradiation. In contrast, the HPT condition, already defect saturated, experiences less irradiation-induced hardening. It is important to note, however, that NC specimens, which comprise a high density of GBs that interact with irradiation-induced defects, generally offer improved irradiation damage resistance compared to their CG counterparts.^[34]

However, the reX condition, which also has a high capacity for the accommodation of defects, exhibits a lesser increase in hardness compared to the 800°C|1h condition, suggesting that the observed hardening is influenced by a mechanism other than just the annealing-induced reduction of defect density. Schuh et al.,^[21] who separately synthesized the same ZrHf- and NbTa-rich BCC phases of the current study's 800°C|1h condition, demonstrated significant hardening of these phases upon HPT-processing (+29% to 3.6 GPa and +81% to 4.7 GPa, respectively). This substantial hardening, caused by HPT-induced defects, suggests that the material has a similarly high capacity to harden due to irradiation-induced defects. The greater hardening observed in the NbTa-rich BCC phase compared to the ZrHf-rich phase highlights its greater hardening susceptibility and likely more significant contribution to the hardening in the 800°C|1h condition.

Across all thermally treated conditions of the NC RHEA, in both irradiation states, a granular structure dominated by grain pullout is observed, indicating intergranular failure as the dominant fracture mechanism, and implying that the grain boundaries in these samples are weaker than the grains themselves. Although no irradiation-induced changes to fracture surfaces are observed in the HPT, 500°C|1h, and 500°C|100h conditions (Figure 7), a distinct change is observed in the 800°C|1h condition (Figure 8). The pre- and post-irradiation fracture surfaces of the 800°C|1h condition follow a similar trend, however, the grains in the unirradiated condition exhibit small ridges along their corners and over their surfaces, potentially suggesting the onset of the formation of dimples. Nevertheless, these features are too small to confirm the hypothesis. Notably, the irradiated structure's fracture surface is bimodal, displaying a portion of whole NbTa-rich grains, alongside regions of rough, irregular surface that are ZrHf-rich (Figure 8b,c). As described earlier, Schuh et al.^[21] found the NbTa-rich BCC phase experienced significantly more hardening than its ZrHf-rich counterpart upon HPT processing which may indicate that irradiation-induced hardening of this phase might lead to increased resistance to transgranular fracture.

The newly discovered HCP phase in the 500°C|100h condition (Figure 2c) raises questions regarding its formation, stability, and influence on the overall mechanical behavior

of the material. Although all other phases exhibit high stability under the applied irradiation profile, the new HCP phase expands from 2.0% in the unirradiated state to 3.4% after irradiation, indicating a heightened propensity for irradiation-induced phase formation which may have contributed to the $\approx 44\%$ ductility loss in the 500°C|100h condition. Further research is required to characterize the role of this HCP phase on mechanical properties of the alloy, particularly under irradiation.

This study emphasizes the impact of phase formation on the irradiation tolerance of HEAs. While recent publications on HEAs have demonstrated their often-exceptional tolerance, this research highlights the significance of investigating the phase formation of such alloys over the desired application temperature range, particularly as most BCC RHEAs are known to form additional phases depending on their thermal history. Future research should explore elevated-temperature irradiation effects (above $0.3 T_M$),^[43–45] emphasizing temperatures relevant to advanced nuclear applications. While significant irradiation-induced hardening and embrittlement are still expected at intermediate temperatures, irradiation-induced defects are more likely to recombine at elevated temperatures, reducing the amount of defect-induced hardening that the material undergoes. However, high-temperature irradiation leads to additional radiation-induced phenomena, such as void swelling, thermal creep, radiation-induced precipitation, and GB embrittlement.^[46] Addressing these factors is essential for a comprehensive understanding of material behavior under conditions encountered in advanced nuclear reactor environments.

5. Conclusion

In this study, the equiatomic TiZrNbHfTa refractory high-entropy alloy (RHEA) was investigated as a candidate material for advanced nuclear applications. The alloy was processed by high-pressure torsion (HPT) to develop a nanocrystalline (NC) structure with a grain size of ≈ 40 nm and subsequently heat-treated at 500 °C for 1 and 100 h, and 800 °C for 1 h, to induce the formation of additional phases. The material conditions were then subjected to He²⁺-ion irradiation to ≈ 0.8 dpa prior to structural and mechanical characterization.

Key outcomes of this research include: 1) The 500°C, 1 h thermal treatment led to the formation of an HCP phase, resulting in increased hardness and yield strength, as well as slightly improved ductility, which is attributed to the relaxation of lattice stresses and a reduction in defect densities relative to the HPT-processed condition; 2) Longer and higher temperature thermal treatments led to grain growth, defect annealing, phase segregation, and decreased solid-solution strengthening, resulting in reduced hardness and yield strength in the 500°C|100h and 800°C|1h conditions compared to the 500°C|1h condition. The 800°C|1h condition exhibited embrittlement and ductility loss due to the formation of an additional BCC phase with poor grain boundary cohesion; 3) Post-irradiation analyses revealed the formation of He-bubbles and an increased defect density across all conditions. The HPT and 500°C|1h conditions displayed no other microstructural changes and, furthermore, exhibited only mild irradiation-induced hardening (≈ 2.5 –6%), highlighting their excellent microstructural stability and good retention of

mechanical properties under the applied irradiation conditions; 4) Using synchrotron XRD, a second HCP phase with lattice parameters of $a = 3.27$ Å and $c = 5.43$ Å was identified in the unirradiated 500°C|100h condition and increased in weight fraction from 2.0% to 3.4% post-irradiation. Despite exhibiting excellent microstructural stability and mild irradiation-induced hardening ($\approx 16\%$), the 500°C|100h condition exhibited a significant loss of ductility ($\approx 44\%$) which may be, in part, attributed to this new phase; 5) Irradiation of the 800°C|1h condition resulted in a $\approx 34\%$ increase in hardness and a $\approx 32\%$ reduction in ductility. These changes are attributed to lower initial defect density, increased susceptibility of the two BCC phases to defect hardening, and poor grain boundary cohesion of the additional BCC phase.

Further studies are recommended to clarify the phase transformation kinetics between the NC condition and its 500°C-treated counterparts, to investigate the bimodal fracture surface of the 800°C|1h condition, to explore the newly discovered HCP phase and its impact on the mechanical properties of the RHEA, and to evaluate the microstructure and mechanical properties of the RHEA after irradiation at temperatures representative of nuclear reactors. Overall, this study highlights the potential of TiZrNbHfTa RHEA for nuclear structural applications, particularly at lower temperatures where detrimental phase formation can be mitigated. Understanding the effects of temperature and phase formation on the irradiation tolerance of RHEAs is critical for the development of materials with improved performance in harsh nuclear environments and the design of next-generation nuclear reactors with enhanced safety, efficiency, and longevity.

Acknowledgements

MM acknowledges the financial support provided by an Australian Government Research Training Program Scholarship and an AINSE Ltd. Residential Student Scholarship, the facilities and assistance provided by Microscopy Australia at the Electron Microscope Unit within the Mark Wainwright Analytical Centre of UNSW Sydney, and the Centre for Accelerator Science at ANSTO. Additionally, this research was conducted, in part, on the Powder Diffraction beamline at the Australian Synchrotron, a part of ANSTO, and the authors thank Dr. Helen Brand for running the samples. BG acknowledges support from the ARC Future Fellowship (project no. FT190100484) and the UNSW Scientia Fellowship schemes. The authors thank Dr. Rob Aughterson and Anastasia Bedford for their assistance in synchrotron sample preparation.

Open access publishing facilitated by University of New South Wales, as part of the Wiley - University of New South Wales agreement via the Council of Australian University Librarians.

Conflict of Interest

The authors declare no conflict of interest.

Data Availability Statement

The data that support the findings of this study are available from the corresponding author upon reasonable request.

Keywords

irradiation tolerance, micromechanical properties, nanocrystalline materials, nuclear structural materials, refractory high-entropy alloys

Received: June 6, 2023

Revised: August 2, 2023

Published online:

- [1] S. J. Zinkle, J. T. Busby, *Mater. Today* **2009**, 12, 12.
- [2] T. Allen, J. Busby, M. Meyer, D. Petti, *Mater. Today* **2010**, 13, 14.
- [3] S. J. Zinkle, G. S. Was, *Acta Mater.* **2013**, 61, 735.
- [4] J.-W. Yeh, S.-K. Chen, S.-J. Lin, J.-Y. Gan, T.-S. Chin, T.-T. Shun, C.-H. Tsau, S.-Y. Chang, *Adv. Eng. Mater.* **2004**, 6, 299.
- [5] Y. Zhang, T. T. Zuo, Z. Tang, M. C. Gao, K. A. Dahmen, P. K. Liaw, Z. P. Lu, *Prog. Mater. Sci.* **2014**, 61, <https://doi.org/10.1016/j.pmatsci.2013.10.001>.
- [6] D. B. Miracle, O. N. Senkov, *Acta Mater.* **2017**, 122, 448.
- [7] M.-H. Tsai, J.-W. Yeh, *Mater. Res. Lett.* **2014**, 2, 107.
- [8] M. Moschetti, A. Xu, B. Schuh, A. Hohenwarter, J.-P. Couzinié, J. J. Kruzic, D. Bhattacharyya, B. Gludovatz, *JOM* **2019**, 72, 130.
- [9] E. J. Pickering, A. W. Carruthers, P. J. Barron, S. C. Middleburgh, D. E. J. Armstrong, A. S. Gandy, *Entropy* **2021**, 23, 98.
- [10] Y. Lu, H. Huang, X. Gao, C. Ren, J. Gao, H. Zhang, S. Zheng, Q. Jin, Y. Zhao, C. Lu, T. Wang, T. Li, *J. Mater. Sci. Technol.* **2019**, 35, 369.
- [11] C. Lu, L. Niu, N. Chen, K. Jin, T. Yang, P. Xiu, Y. Zhang, F. Gao, H. Bei, S. Shi, M.-R. He, I. M. Robertson, W. J. Weber, L. Wang, *Nat. Commun.* **2016**, 7, 13564.
- [12] D.-H. Lee, M.-Y. Seok, Y. Zhao, I.-C. Choi, J. He, Z. Lu, J.-Y. Suh, U. Ramamurty, M. Kawasaki, T. G. Langdon, J. Jang, *Acta Mater.* **2016**, 109, 314.
- [13] D. Chen, S. Zhao, J. Sun, P. Tai, Y. Sheng, Y. Zhao, G. Yeli, W. Lin, S. Liu, W. Kai, J.-J. Kai, *J. Nucl. Mater.* **2019**, 526, 151747.
- [14] D. Li, N. Jia, H. Huang, S. Chen, Y. Dou, X. He, W. Yang, Y. Xue, Z. Hua, F. Zhang, L. Wang, K. Jin, H. Cai, *J. Nucl. Mater.* **2021**, 552, 153023.
- [15] M. Moschetti, P. A. Burr, E. Obbard, J. J. Kruzic, P. Hosemann, B. Gludovatz, *J. Nucl. Mater.* **2022**, 567, 153814.
- [16] F. Otto, Y. Yang, H. Bei, E. P. George, *Acta Mater.* **2013**, 61, 2628.
- [17] M. Caro, L. K. Béland, G. D. Samolyuk, R. E. Stoller, A. Caro, *J. Alloys Compd.* **2015**, 648, 408.
- [18] Y. Zhang, G. M. Stocks, K. Jin, C. Lu, H. Bei, B. C. Sales, L. Wang, L. K. Béland, R. E. Stoller, G. D. Samolyuk, M. Caro, A. Caro, W. J. Weber, *Nat. Commun.* **2015**, 6, 8736.
- [19] O. N. Senkov, J. M. Scott, S. V. Senkova, D. B. Miracle, C. F. Woodward, *J. Alloys Compd.* **2011**, 509, 6043.
- [20] O. N. Senkov, J. M. Scott, S. V. Senkova, F. Meisenkothen, D. B. Miracle, C. F. Woodward, *J. Mater. Sci.* **2012**, 47, 4062.
- [21] B. Schuh, B. Völker, J. Todt, N. Schell, L. Perrière, J. Li, J. P. Couzinié, A. Hohenwarter, *Acta Mater.* **2018**, 142, 201.
- [22] C. R. F. Azevedo, *Eng. Fail. Anal.* **2011**, 18, 1943.
- [23] N. D. Stepanov, N. Y. Yurchenko, S. V. Zharebtsov, M. A. Tikhonovsky, G. A. Salishchev, *Mater. Lett.* **2018**, 211, 87.
- [24] S. Y. Chen, Y. Tong, K.-K. Tseng, J.-W. Yeh, J. D. Poplawsky, J. G. Wen, M. C. Gao, G. Kim, W. Chen, Y. Ren, R. Feng, W. D. Li, P. K. Liaw, *Scr. Mater.* **2019**, 158, 50.
- [25] R. Z. Valiev, T. G. Langdon, *Prog. Mater. Sci.* **2006**, 51, 881.
- [26] S. Chen, K.-K. Tseng, Y. Tong, W. Li, C.-W. Tsai, J.-W. Yeh, P. K. Liaw, *J. Alloys Compd.* **2019**, 795, 19.
- [27] O. N. Senkov, S. L. Semiatin, *J. Alloys Compd.* **2015**, 649, 1110.
- [28] D. S. Aidhy, Y. Zhang, W. J. Weber, *Scr. Mater.* **2014**, 83, 9.
- [29] H. Shahmir, J. He, Z. Lu, M. Kawasaki, T. G. Langdon, *Mater. Sci. Eng. A* **2016**, 676, 294.
- [30] J. Zhou, M. I. Islam, S. Guo, Y. Zhang, F. Lu, *J. Phys. Chem. C* **2021**, 125, 3509.
- [31] T. S. Orlova, N. V. Skiba, A. M. Mavlyutov, M. Y. Murashkin, R. Z. Valiev, M. Y. Gutkin, *Rev. Adv. Mater. Sci.* **2018**, 57, 224.
- [32] D. Hull, D. J. Bacon, *Introduction to Dislocations*, Elsevier, Amsterdam **2011**.
- [33] T. H. Courtney, *Mechanical Behavior of Materials*, Waveland Press, Long Grove, Illinois **2005**.
- [34] A. Etienne, B. Radigue, N. J. Cunningham, G. R. Odette, R. Valiev, P. Pareige, *Ultramicroscopy* **2011**, 111, 659.
- [35] G. A. Vetterick, J. Gruber, P. K. Suri, J. K. Baldwin, M. A. Kirk, P. Baldo, Y. Q. Wang, A. Misra, G. J. Tucker, M. L. Taheri, *Sci. Rep.* **2017**, 7, 12275.
- [36] J. Laakmann, P. Jung, W. Uelhoff, *Acta Metall.* **1987**, 35, 2063.
- [37] P. L. Lane, P. J. Goodhew, *Philos. Mag. A* **1983**, 48, 965.
- [38] T. Wei, H. Zhu, M. Ionescu, P. Dayal, J. Davis, D. Carr, R. Harrison, L. Edwards, *J. Nucl. Mater.* **2015**, 459, 284.
- [39] H. Ullmaier, *Nucl. Fusion* **1984**, 24, 1039.
- [40] Y. Zhang, T. Egami, W. J. Weber, *MRS Bull.* **2019**, 44, 798.
- [41] J. C. Haley, S. A. Briggs, P. D. Edmondson, K. Sridharan, S. G. Roberts, S. Lozano-Perez, K. G. Field, *Acta Mater.* **2017**, 136, 390.
- [42] D. J. Barber, *Ultramicroscopy* **1993**, 52, 101.
- [43] P. Kumar, M. Kawasaki, T. G. Langdon, *J. Mater. Sci.* **2016**, 51, 7.
- [44] M. Nastar, F. Soisson, *Comprehensive Nuclear Materials*, Elsevier, Amsterdam **2012**, p. 471.
- [45] E. A. Kenik, J. T. Busby, *Mater. Sci. Eng.* **2012**, 73, 67.
- [46] J. E. Pawel, A. F. Rowcliffe, G. E. Lucas, S. J. Zinkle, *J. Nucl. Mater.* **1996**, 239, 126.
- [47] Y.-F. Jia, Y.-Y. Cui, F.-Z. Xuan, F. Yang, *RSC Adv.* **2017**, 7, 35655.